Functionalized Nanocellulose-Integrated Heterolayered Nanomats toward Smart Battery Separators

Jung-Hwan Kim,[†1] Minsu Gu,[†1] Do Hyun Lee,[1] Jeong-Hoon Kim,[1] Yeon-Su Oh,[1] Sa Hoon Min,[1] Byeong-Su Kim[1,2]* and Sang-Young Lee[1]**

[1]Department of Energy Engineering, School of Energy and Chemical Engineering and [2]Department of Chemistry, School of Natural Science, Ulsan National Institute of Science and Technology (UNIST), Ulsan 44919, Republic of Korea

[†] These authors contributed equally to this work.

E-mail: minshu21@unist.ac.kr (S. H. Min); bskim19@unist.ac.kr (B.-S. Kim); syleek@unist.ac.kr (S.-Y. Lee)

Methods:

Synthesis of terpyridine (TPY) ligand. Terpyridine was synthesized and modified using the protocol reported previously in the literature.[1] Potassium hydroxide (KOH) pellets (1.15 g) and 23 mL of ammonia (28%) were added to a mixture of 2-acetylpyridine (1.685 mL) and 4-cyanobenzaldehyde (0.98 g) in anhydrous ethanol (50 mL), and the resulting mixture was stirred for 24 h at 34 ºC. The mixture was subsequently cooled in an ice bath and processed using vacuum filtration with a washing step using ice-cold anhydrous ethanol. The filtered powder was recrystallized with anhydrous ethanol, resulting in a pure white powder. One gram of the obtained white powder dissolved in 35 mL of THF was slowly added via a syringe pump to a solution of lithium aluminium hydride (0.50 g) dissolved in 35 mL of THF. The mixture was stirred for 12 h at 25 ºC under a nitrogen atmosphere. After the reaction, an additional 50 mL of THF was added and the mixture was subsequently processed using vacuum filtration with vigorous washing with THF. The filtered yellowish solution was evaporated using a rotary evaporator. The resulting powder was dissolved in dichloromethane (DCM), and HCl gas was then pumped into the solution for 90 min. The formed precipitate was filtered and dissolved in deionized (DI) water. To further purify the synthesized TPY, a 0.10 M NaOH solution was added to the aqueous solution and extracted with DCM. The extract was evaporated and then dissolved in 0.10 M HCl solution to a concentration of 30 mg mL^{-1}.

Synthesis of functionalized nanocellulose with TPY (TPY-CNF). The nanocellulose suspension was produced by repeated high-pressure homogenization of pretreated wood cellulose powders (particle size ~45 µm, KC Flock, Nippon Paper Chemicals) in water. The detailed procedure for preparing the CNF suspension is described in our previous publications.[2] To oxidize the nanocellulose, a 0.50 wt% cellulose suspension (100 mL) was

mixed with 2,2,6,6-tetramethylpiperidine-1-oxyl (TEMPO, 14.75 mg), sodium bromide (NaBr, 162 mg) and 5 wt% sodium hypochlorite solution (NaClO, 10 mL) for 6 h. The resulting mixture was washed with DI water by centrifugation. This oxidized nanocellulose suspension (50 mL) was then reacted with the as-synthesized TPY solution (4.0 mL) for 12 h in the presence of *N*-ethyl-*N′*-(3-dimethylaminopropyl)carbodiimide methiodide (EDC, 238 mg). The resulting suspension was washed with DI water by centrifugation.

DFT calculations. To compare the binding energy of Mn^{2+} complexes, we performed DFT calculations using the Gaussian 09 program.[3] $Mn^{2+}(PP_3)$, Mn^{2+}(Glc), and Mn^{2+}(TPY) were introduced as model complexes for the PP, CNF, and TPY, respectively. The spin multiplicity for the ground state of Mn^{2+} complexes was set to sextet. Geometry optimizations were calculated at the level of B3LYP/6-31G(d,p), and accurate single-point energies were obtained at the level of B3LYP/6-311+G(2d,2p) from the optimized geometries. The basis set superposition error (BSSE) corrections were also considered in the binding energy calculations.

MD simulations. To test the binding stability of Mn^{2+} ions, we performed all-atom MD simulations using the AMBER force field.[4,5] Microcrystalline models (approximately 6 nm in both length and width) of syndiotactic PP, cellulose Iβ, and cellulose Iβ with 4 TPY groups were placed in parallel with the *xy*-plane of the simulation box. In the case of cellulose, the (010) exposed surface was built using the Cellulose-Builder toolkit.[6] The Mn^{2+} ions were set to be positioned at each model surface, and the simulation box was then filled with 1,600 EC molecules and 8 PF_6^- ions. The generalized AMBER forcefield (GAFF) parameters[4] were used for the PP, EC, and TPY group, and the cellulose was parameterized by the GLYCAM06 forcefield.[5] The PF_6^- ion model was taken from the literature.[7] All partial charges on the PP, EC, and TPY group were calculated using the AM1-BCC method in

AmberTools14.[8] The MD simulations and visualizations were performed using the Amber14 and VMD software packages,[9] respectively. After the energy of the initial conformation was minimized, each system was relaxed by a 100-ps canonical (NVT) and 500-ps isothermal-isobaric (NPT) MD simulation at 333 K. For the production run, long NPT MD simulations were calculated at 333 K and P = 1 bar using the Langevin thermostat with a collision frequency of 1.0 ps^{-1} and the Berendsen barostat with a coupling constant of 2.0 ps. The cutoff distance of 1.0 nm and the particle mesh Ewald (PME) method were applied to the short-range nonbonding interactions and the long-range electrostatic interactions, respectively. All bond lengths involving H atoms were constrained with the SHAKE algorithm,[10] and a time step of 2 fs was used.

Structural design and fabrication of the c-mat separator. To fabricate the electrospun macroporous mat, we used electrospinning with PVP/PAN blends. The blended PAN (molecular weight = 150,000 g mol^{-1}) and PVP (molecular weight = 1,300,000 g mol^{-1}) solution was prepared by dissolving the polymers in dimethylacetamide (DMAc) at 70 ºC for 12 h, where the total polymer concentration was 20 wt.% and the relative composition ratio of PVP/PAN was 50/50 (w/w). The electrospinning conditions were 8.0 kV and a feed rate of 3.5 μL min^{-1}. The resulting electrospun PVP/PAN mat was collected on a stainless steel plate positioned 10 cm from the nozzles. After being roll-pressed at room temperature, a freestanding macroporous electrospun mat (thickness ~19 μm) was produced. The c-mat separators were fabricated via a simple vacuum-assisted infiltration process. The TPY-CNF suspension was poured onto a PVP/PAN mat positioned inside a porcelain Büchner funnel and then subjected to a vacuum to infiltrate the porous mat, leading to the formation of a hierarchical/asymmetric porous structure. The thickness of the TPY-CNF layer was

controlled by varying the amount of the TPY-CNF suspension. The final c-mat separator (thickness ~20 μm) was obtained with a 1-μm-thick TPY-CNF layer. A commercial PP/PE/PP separator (thickness ~20 μm, Celgard) was chosen as the control sample.

Characterizations of TPY-CNF. The ^{1}H NMR spectra of TPY were acquired using a VNMRS 600 spectrometer operated at 600 MHz; the samples were dissolved in DMSO solvent. A mass analysis of TPY was carried by mass spectroscopy (450-GC & 320-MS, Bruker). Fourier transform infrared (FT-IR) spectra were collected using an FT-IR spectrophotometer (670-IR, Varian). X-ray photoelectron spectroscopy (XPS, Thermo Fisher, K-alpha) was used to detect the chemical state of TPY-CNF.

Structural/physicochemical characterizations of the c-mat separator. The surface and cross-sectional morphologies of the separators were characterized by field emission scanning electron microscopy (FE-SEM, Hitachi) in conjunction with energy-dispersive X-ray spectroscopy (EDS). The pore size distribution of the c-mat separator was measured using mercury intrusion porosimetry (AutoPore IV 9500, Micromeritics Instrument Corp.). The thermal shrinkage of the separators was evaluated by measuring their (area-based) dimensional change after exposure to 150 ºC for 0.5 h. For the electrochemical characterization of the separators, a liquid electrolyte of 1 M $LiPF_6$ in EC/DEC (1/1 (v/v), Soulbrain) was employed. The electrolyte wettability of the separators was quantitatively estimated by measuring the separators' electrolyte immersion height.

Electrochemical properties of the c-mat separator and its application to lithium-ion batteries. The electrochemical stability window of the separators was measured by a linear sweep voltammetry experiment performed on a working electrode of stainless steel and a counter and reference electrode of lithium metal at a scan rate of 1.0 mV s^{-1}. The open-circuit

voltage (OCV) drop in the fully charged cell (at a current density of 0.2C) was monitored as a function of elapsed time. The ionic conductivity of the separator was examined by AC impedance analysis (VSP classic, Bio-Logic) over the frequency range from 10^{-2} to 10^{6} Hz. A pouch-type cell (width × length = 30 × 40 mm^2) was assembled by sandwiching a separator between the LMO cathode (LMO/carbon black/PVdF = 92/3/5 w/w/w, areal mass loading = 17 mg cm^{-2}) and the Li metal anode (the TPY-CNF top layer was in contact with the LMO cathode while the PVP/PAN support layer faced the Li metal anode), and the cell was activated by being filled with the liquid electrolyte (1 M $LiPF_6$ in EC/DEC = 1/1 v/v). The cell performance was investigated using a cycle tester (PNE Solution) at 25 and 60 °C under various charge/discharge conditions.

Figure S1. (a) ^{1}H NMR spectra and (b) mass analysis of TPY.

Figure S2. SEM images of the PP/PE/PP separator.

Figure S3. Discharge profiles of cells assembled with (a) PP/PE/PP separator and c-mat separator with TPY-CNF layers with thicknesses of (b) 1 μm, (c) 3 μm and (d) 10 μm.

Figure S4. A photograph showing the structural disruption of the electrospun mat after the mat was immersed in a liquid electrolyte (1 M $LiPF_6$ in EC/DEC = 1/1 (v/v)): (a) PVP electrospun mat and (b) PVP/PAN electrospun mat.

Figure S5. Variation in the XPS spectra (characteristic peak of nitrogen atoms) of PVP/PAN or PAN films after the films were swelled in a liquid electrolyte (1 M $LiPF_6$ in EC/DEC = 1/1 v/v) containing dissolved HF (100 ppm): (a) PVP/PAN film and (b) PAN film.

Figure S6. Characterization of the separator properties. (a) Linear sweep voltammograms. (b) Electrolyte wettability. (c) Effect of polar electrolyte (here, 1 M $LiPF_6$ in EC/PC = 1/1 (v/v)) on wettability of separators and charge/discharge performance of cells incorporating PP/PE/PP separator and c-mat separator. (d) Thermal shrinkage after exposure to 150 ºC/0.5 h.

Figure S7. Comparison of the cell performance (at room temperature) of the c-mat and PP/PE/PP separators: (a) Discharge rate capability (LMO cathode/Li metal anode), (b) Discharge rate capability (LCO cathode/natural graphite anode), and (c) Cycling performance (LMO cathode/Li metal anode).

Figure S8. (a) Impedance spectra and (b) summary of the fitting results for the c-mat and PP/PE/PP separators after cycling (at 60 ºC). The inset in part (a) represents the equivalent circuit. Units of R_b, R_{sf} and R_{ct} are in ohms. R_b is the bulk resistance, R_{sf} is the surface

resistance, and R_{ct} is the charge transfer resistance. CPE_{sf} and CPE_{ct} are the constant phase elements at high and low frequencies, respectively.

Figure S9. SEM images showing the long-term structural stability (after 100 charge/discharge cycles at 60 °C) of the c-mat separator: (a) TPY-CNF top layer and (b) PVP/PAN support layer.

Figure S10. Comparison of high-temperature (60 ºC) cycling performance between the cell (I) and cell (II), in which the TPY-CNF top layer was in contact with the LMO cathode (for cell (I)) and positioned toward the Li metal anode (for cell (II)).

Table S1. Basic separator properties of the c-mat and PP/PE/PP separators.

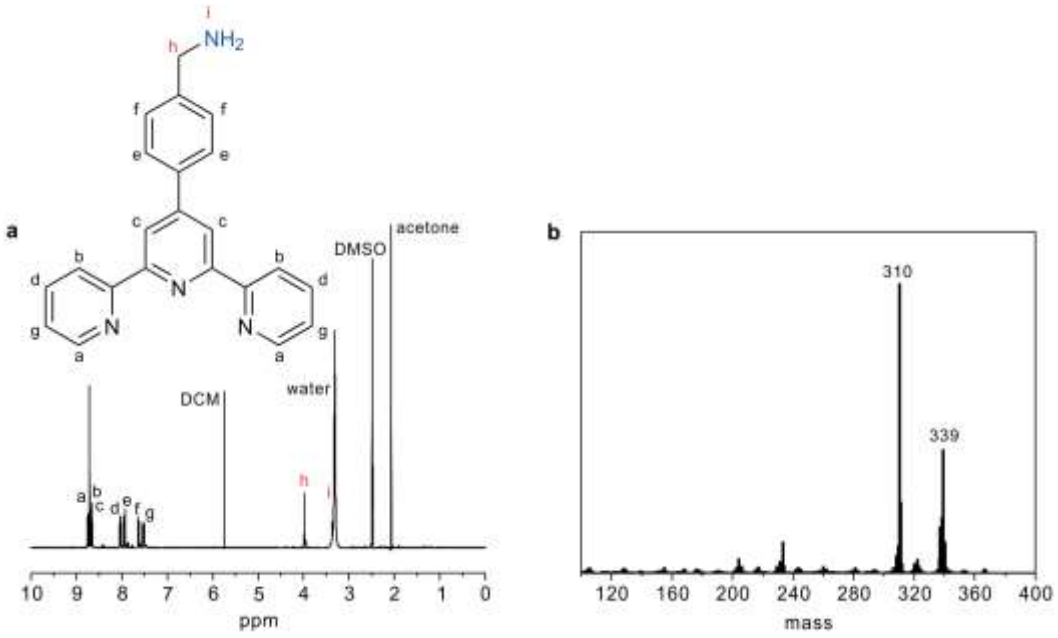

Figure S1. (a) ^{1}H NMR spectra and (b) mass analysis of TPY.

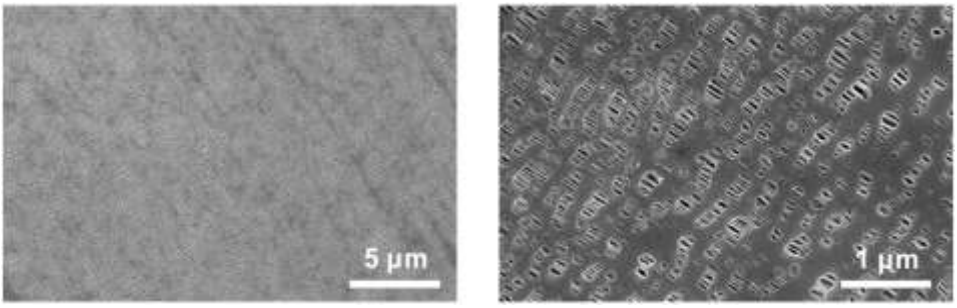

Figure S2. SEM images of the PP/PE/PP separator.

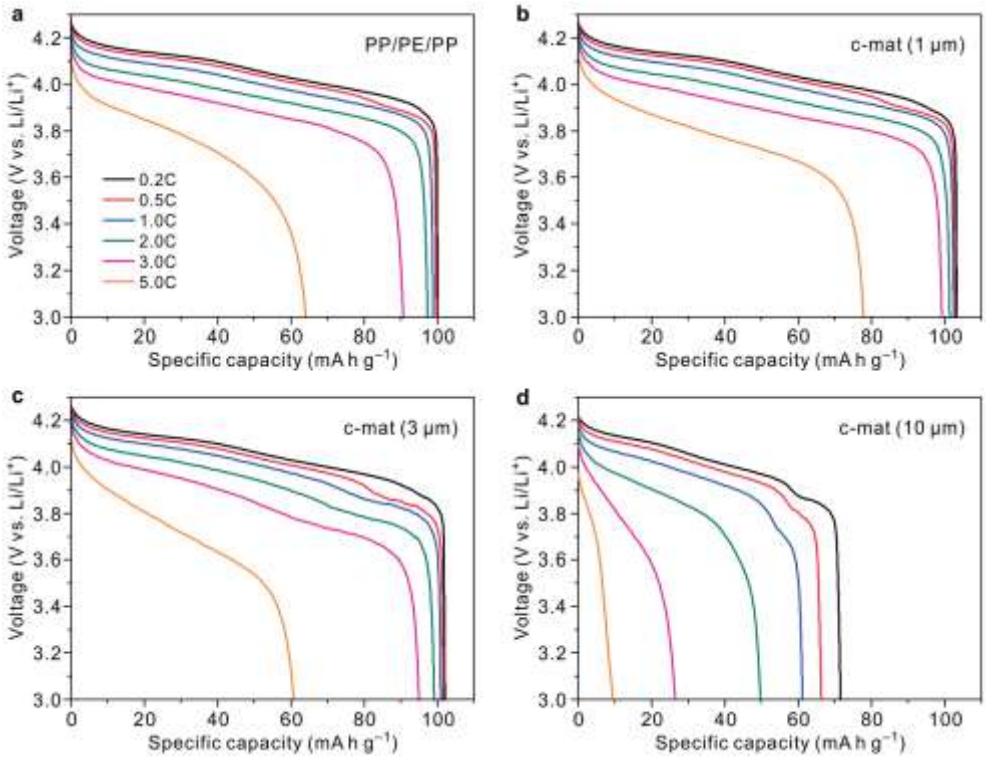

Figure S3. Discharge profiles of cells assembled with (a) PP/PE/PP separator and c-mat separator with TPY-CNF layers with thicknesses of (b) 1 μm, (c) 3 μm and (d) 10 μm.

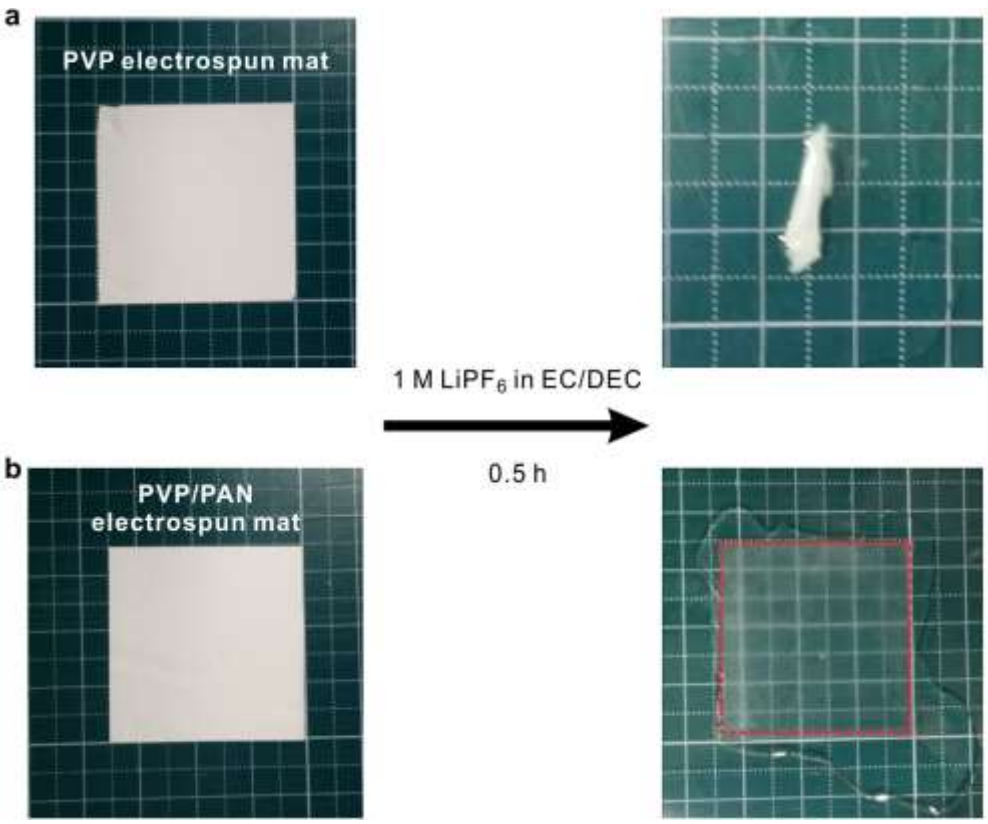

Figure S4. A photograph showing the structural disruption of the electrospun mat after the mat was immersed in a liquid electrolyte (1.0 M $LiPF_6$ in EC/DEC = 1/1 (v/v)): (a) PVP electrospun mat and (b) PVP/PAN electrospun mat.

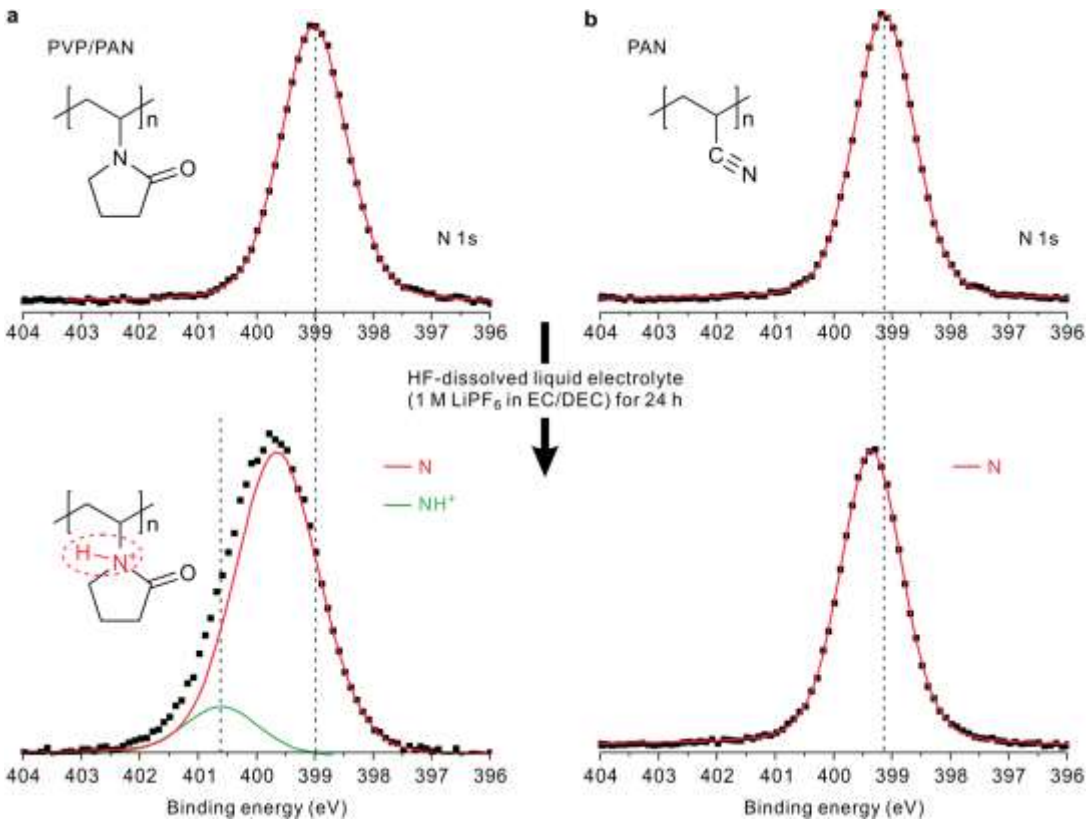

Figure S5. Variation in the XPS spectra (characteristic peak of nitrogen atoms) of PVP/PAN or PAN films after the films were swelled in a liquid electrolyte (1.0 M $LiPF_6$ in EC/DEC = 1/1 v/v) containing dissolved HF (100 ppm): (a) PVP/PAN film and (b) PAN film.

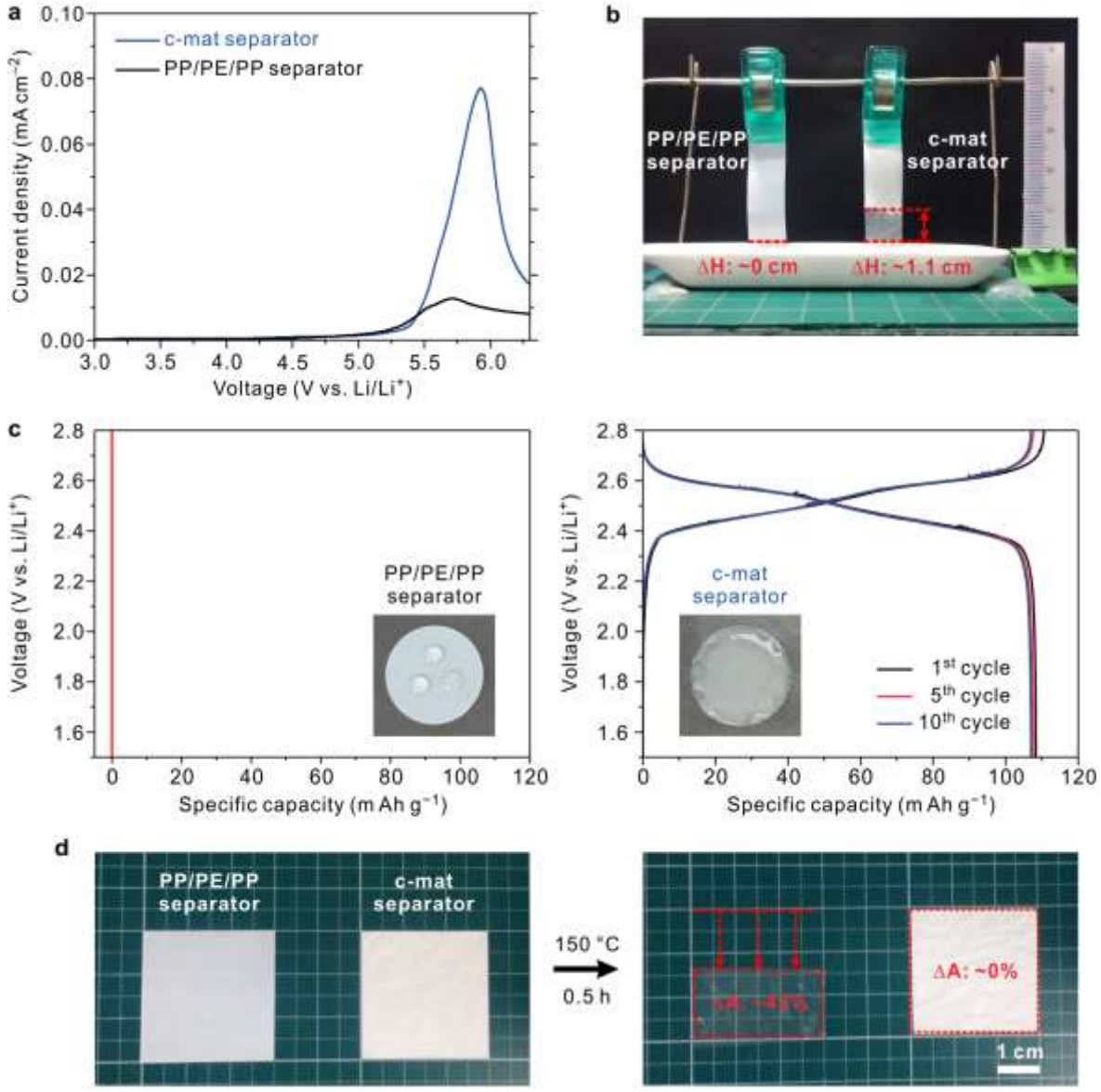

Figure S6. Characterization of the separator properties. (a) Linear sweep voltammograms. (b) Electrolyte wettability. (c) Effect of polar electrolyte (here, 1.0 M $LiPF_6$ in EC/PC = 1/1 (v/v)) on wettability of separators and charge/discharge profiles of cells incorporating PP/PE/PP separator and c-mat separator. (d) Thermal shrinkage after exposure to 150 ºC/0.5 h.

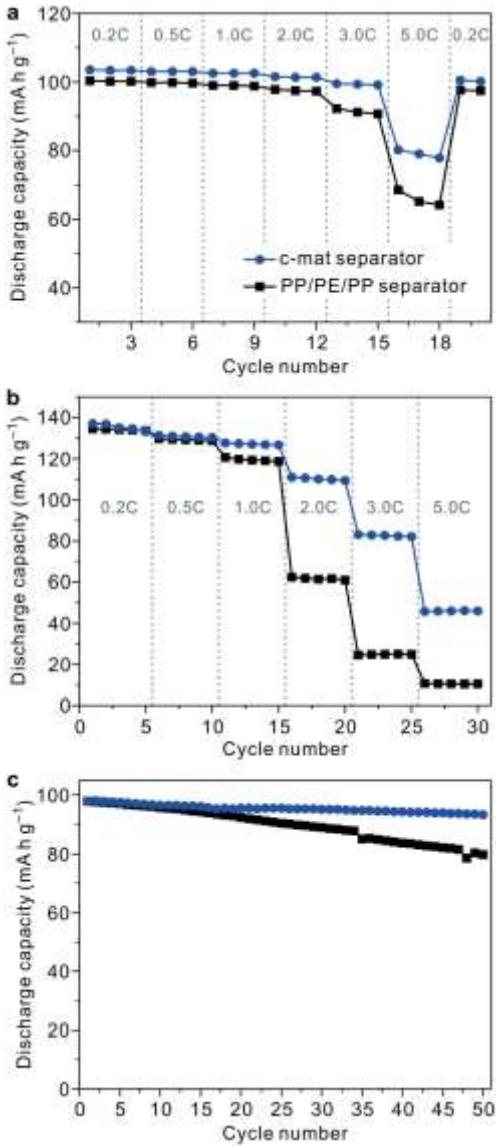

Figure S7. Comparison of the cell performance (at room temperature) of the c-mat and PP/PE/PP separators: (a) Discharge rate capability (LMO cathode/Li metal anode), (b) Discharge rate capability (LCO cathode/natural graphite anode), and (c) Cycling performance (LMO cathode/Li metal anode).

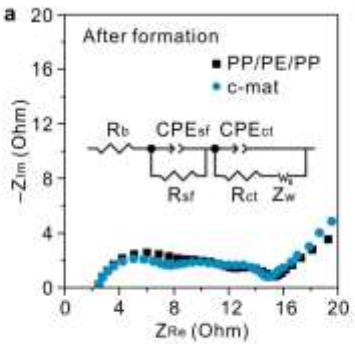

b

Sample	After 1st cycle			After 100th cycle		
	R_b	R_{sf}	R_{ct}	R_b	R_{sf}	R_{ct}
c-mat	1.9	4.1	11.1	4.9	12.9	27.1
PP/PE/PP	2.4	4.3	11.7	9.0	58.3	222.8

Figure S8. (a) Impedance spectra and (b) summary of the fitting results for the c-mat and PP/PE/PP separators after cycling (at 60 ºC). The inset in part (a) represents the equivalent circuit. Units of R_b, R_{sf} and R_{ct} are in ohms. R_b is the bulk resistance, R_{sf} is the surface resistance, and R_{ct} is the charge transfer resistance. CPE_{sf} and CPE_{ct} are the constant phase elements at high and low frequencies, respectively.

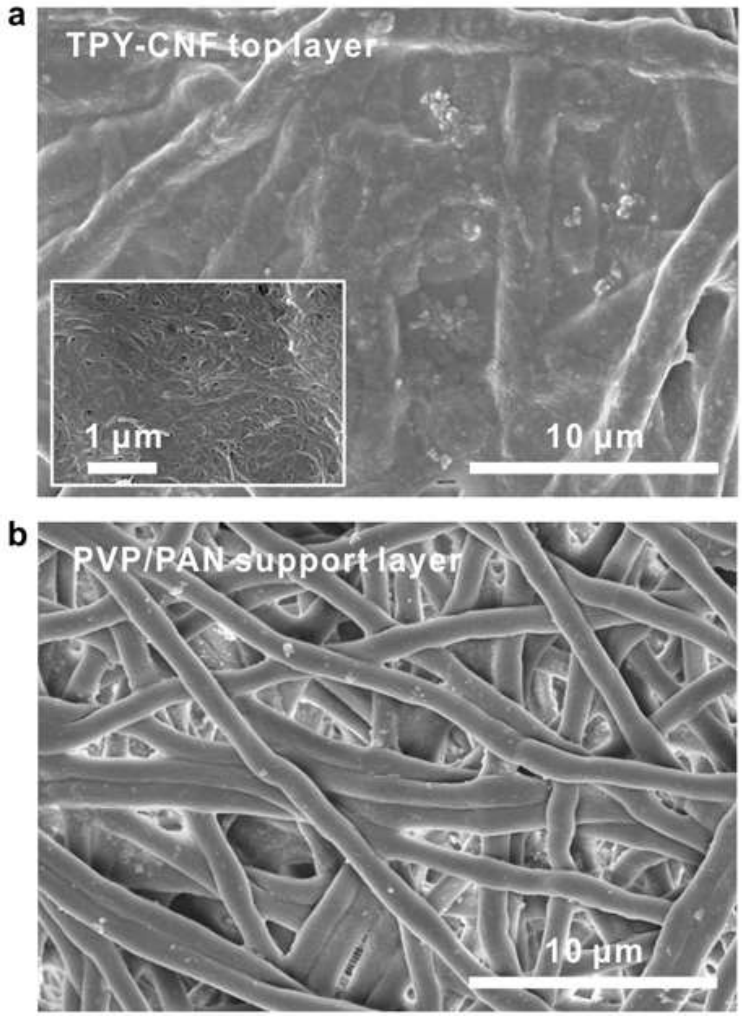

Figure S9. SEM images showing the long-term structural stability (after 100 charge/discharge cycles at 60 °C) of the c-mat separator: (a) TPY-CNF top layer and (b) PVP/PAN support layer.

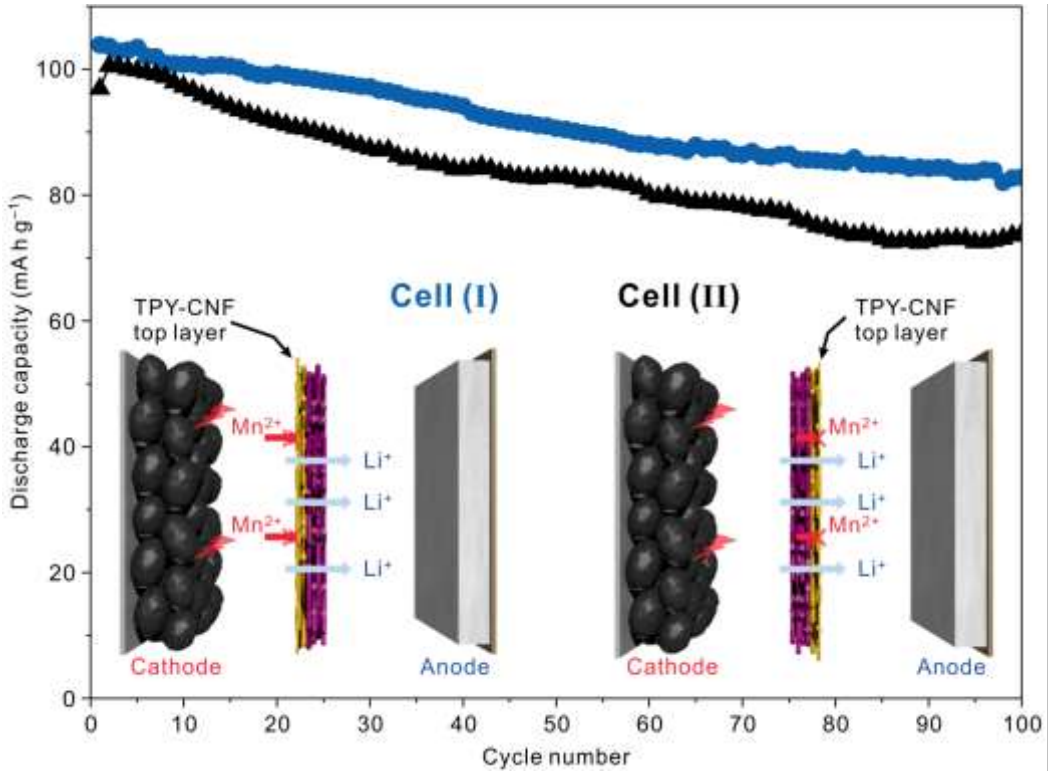

Figure S10. Comparison of high-temperature (60 ºC) cycling performance between the cell (I) and cell (II), in which the TPY-CNF top layer was in contact with the LMO cathode (for cell (I)) and positioned toward the Li metal anode (for cell (II)).

Table S1. Basic separator properties of the c-mat and PP/PE/PP separators.

	Thickness	Gurley value	Porosity	Ionic conductivity
	μm	s 100 cc air^{-1}	%	mS cm^{-1}
c-mat separator	~20	10	~65	0.75
PP/PE/PP separator	~20	500	~40	0.6

REFERENCES

1. Kong, B.; Zhu, A.; Ding, C.; Zhao, X.; Li, B.; Tian, Y. *Adv. Mater.* **2012,** *24,* 5844–5848.

2. Chun, S.-J.; Choi, E.-S.; Lee, E.-H.; Kim, J. H.; Lee, S.-Y.; Lee, S.-Y. *J. Mater. Chem.* **2012,** *22,* 16618–16626.

3. Frisch, M. J.; Trucks, G. W.; Schlegel, H. B.; Cheeseman, J. R.; Scalmani, G.; Barone, V.; Mennucci, B.; Petersson, G. A. *Gaussian 09, revision C. 01.*; Gaussian Inc., 2010.

4. Wang, J.; Wolf, R. M.; Caldwell, J. W.; Kollman, P. A.; Case, D. A. *J. Comput. Chem.* **2004,** *25,* 1157–1174.

5. Kirschner, K. N.; Yongye, A. B.; Tschampel, S. M.; González-Outeiriño, J.; Daniels, C. R. Foley, B. L.; Woods, R. J. *J. Comput. Chem.* **2008,** *29,* 622–655.

6. Gomes, T. C. F.; Skaf, M. S. *J. Comput. Chem.* **2012,** *33,* 1338–1346.

7. Liu, Z.; Huang, S.; Wang, W. *J. Phys. Chem. B* **2004,** *108,* 12978–12989.

8. Case, D. A.; Babin, V. Berryman, J. T.; Betz, R. M.; Cai, Q.; Cerutti, D. S.; Cheatham III, T. E.; Darden, T. A.; Duke, R. E.; Gohlke, H. AMBER 14.; University of California, 2014.

9. Humphrey, W.; Dalke, A.; Schulten, K. *J. Mol. Graph.* **1996,** *14,* 33–38.

10. Ryckaert, J.-P.; Ciccotti, G.; Berendsen, H. J. C. *J. Comput. Phys.* **1977,** *23,* 327–341.